

Open Research Online

The Open University's repository of research publications and other research outputs

Replacement reactions and deformation by dissolution and precipitation processes in amphibolites

Journal Item

How to cite:

Giuntoli, Francesco; Menegon, Luca and Warren, Clare J. (2018). Replacement reactions and deformation by dissolution and precipitation processes in amphibolites. *Journal of Metamorphic Geology*, 36(9) pp. 1263–1286.

For guidance on citations see [FAQs](#).

© 2018 John Wiley Sons Ltd.



<https://creativecommons.org/licenses/by-nc-nd/4.0/>

Version: Accepted Manuscript

Link(s) to article on publisher's website:
<http://dx.doi.org/doi:10.1111/jmg.12445>

Copyright and Moral Rights for the articles on this site are retained by the individual authors and/or other copyright owners. For more information on Open Research Online's data [policy](#) on reuse of materials please consult the policies page.

oro.open.ac.uk

Replacement reactions and deformation by dissolution and precipitation processes in amphibolites

Francesco Giuntoli^{a*}, Luca Menegon^a, Clare J. Warren^b

^a School of Geography, Earth and Environmental Sciences, Plymouth University, Plymouth PL4 8AA, UK (francesco.giuntoli@gmail.com)

^b School of Environment, Earth and Ecosystem Sciences, Faculty of Science, Technology, Engineering and Mathematics, The Open University, Walton Hall, Milton Keynes, MK7 6AA, UK

Short title: dissolution-precipitation in amphibolites

Abstract

The deformation of the middle to lower crust in collisional settings occurs via deformation mechanisms that vary with rock composition, fluid content, pressure and temperature. These mechanisms are responsible for the accommodation of large tectonic transport distances during nappe stacking and exhumation. Here we show that fracturing and fluid flow triggered coupled dissolution-precipitation and dissolution-precipitation creep processes, which were responsible for the formation of a mylonitic microstructure in amphibolites. This fabric is developed over a crustal thickness of >500 m in the Lower Seve Nappe (Scandinavian Caledonides). Amphibolites display a mylonitic foliation that wraps around albite porphyroclasts appearing dark in panchromatic cathodoluminescence. The albite porphyroclasts were dissected and fragmented by fractures preferentially developed along the (001) cleavage planes, and display lobate edges with embayments and peninsular features. Two albite/oligoclase generations, bright in cathodoluminescence, resorbed and overgrew the porphyroclasts, sealing the fractures. Electron backscattered diffraction shows that the two albite/oligoclase generations grew both pseudomorphically and topotaxially at the expense of the albite porphyroclasts, and epitaxially around them. These two albite/oligoclase generations also grew as neoblasts elongated parallel to the mylonitic foliation. The amphibole crystals experienced a similar microstructural evolution, as evidenced by corroded ferrohornblende cores surrounded by ferrotschermakite rims that preserve the same crystallographic orientation of the cores. Misorientation maps highlight how misorientations in amphibole are related to displacement along fractures perpendicular to its c-axis. No crystal plasticity is observed in either mineral species. Plagioclase and amphibole display a crystallographic preferred orientation that is the result of topotaxial growth on parental grains and nucleation of new grains with a similar crystallographic orientation. Amphibole and plagioclase thermobarometry constrains the mylonitic foliation development to the epidote amphibolite facies (~600°C, 0.75-0.97 GPa). Our results demonstrate that at middle to lower crustal levels the presence

This article has been accepted for publication and undergone full peer review but has not been through the copyediting, typesetting, pagination and proofreading process, which may lead to differences between this version and the Version of Record. Please cite this article as doi: 10.1111/jmg.12445

This article is protected by copyright. All rights reserved.

of H₂O-rich fluid at grain boundaries facilitates replacement reactions by coupled dissolution-precipitation and favours deformation by dissolution-precipitation creep over dislocation creep in plagioclase and amphibole.

Keywords

Replacement reactions, dissolution-precipitation processes, Caledonides, electron backscatter diffraction, X-ray mapping.

1 | INTRODUCTION

The thermo-mechanical properties of the middle to lower crust exert a fundamental control on the structure of orogenic belts, and on the amount and style of shortening during continental collision (e.g. Jackson, Austrheim, McKenzie, & Priestley, 2004; Mouthereau, Watts, & Burov, 2013). In particular, how strain is distributed vertically and horizontally in orogenic belts is one of the more important questions in crustal dynamics, and one that can be addressed by investigating the deformation mechanisms associated with the accumulation of hundreds of kilometre tectonic transport distances along thrust faults during mountain building processes (e.g. Füsseis & Handy, 2008; Gilotti, 1989; Mouthereau, Lacombe, & Vergés, 2012; Northrup, 1996; Royden, 1996).

In particular, the deformation processes and rheology of mafic shear zones are the subject of considerable debate, because their main mineral constituents (e.g. plagioclase, amphibole, clinopyroxene) are expected to be rheologically strong at middle to lower crustal conditions (e.g. Bürgmann & Dresen, 2008). Thus, the weakening of mafic assemblages along major thrust faults developed at middle to lower crustal conditions seems to critically depend on the occurrence of metamorphic reactions, which can result in the formation of rheologically weaker phases, or in the formation of fine-grained material able to deform by grain size sensitive creep, or in both (e.g. Rutter & Brodie, 1992; Brander, Svahnberg, & Piazzolo, 2012; Okudaira, Shigematsu, Harigane, & Yoshida, 2017). Furthermore, the presence of H₂O-rich fluid at the grain boundary typically facilitates dissolution and precipitation processes, which have been identified as the main deformation mechanisms in different mid-crustal lithologies, and up to high temperature and high pressure conditions (Carmichael, 1969; Giuntoli, Lanari, & Engi, 2018; Gratier, Dysthe, & Renard, 2013; Imon, Okudaira, & Fujimoto, 2002; Imon, Okudaira, & Kanagawa, 2004; McAleer et al., 2017; Menegon, Pennacchioni, & Spiess, 2008; Mukai, Austrheim, Putnis, & Putnis, 2014; Putnis, 2009; Rutter, 1983; Stokes, Wintsch, & Southworth, 2012; Wassmann & Stöckhert, 2013; Wassmann, Stöckhert, & Trepmann, 2011; Wintsch & Yi, 2002). Two main dissolution and precipitation processes can be distinguished: coupled dissolution-precipitation and dissolution-precipitation creep. Coupled dissolution-precipitation results in the pseudomorphic (maintaining the size and shape of the pre-existing phase) and topotaxial (using the orientation of the pre-existing phase) replacement of a parent phase by a product phase from a reaction interface (e.g. Putnis, 2002; Ruiz-Agudo, Putnis, & Putnis, 2014). Dissolution-precipitation creep includes the transport of the chemical constituents from the dissolution sites, of locally high normal stress, to the precipitation site, of locally low normal stress (e.g. Imon et al., 2002; Imon et al., 2004; Mukai et al., 2014; Wassmann et al., 2011). Both processes invariably require the presence of a fluid.

Porosity is another essential requirement for the operation of dissolution and precipitation processes, as it provides the necessary fluid pathways. Porosity may develop during replacement reactions due to molar volume differences between the dissolved and the precipitated minerals (Engvik, Putnis, Gerald, & Austrheim, 2008), or from dehydration reactions and associated fracturing (Plumper, John, Podladchikov, Vrijmoed, & Scambelluri, 2017). Other porosity-generating mechanisms in metamorphic environments include dilatancy at grain boundaries (Tullis, Yund, & Farver, 1996), fracturing (e.g. Brander et al., 2012), and creep cavitation in fine-grained ultramylonites deforming by grain size sensitive creep (Füsseis, Regenauer-Lieb, Liu, Hough, & De Carlo, 2009; Menegon, Füsseis, Stünitz, & Xiao, 2015).

Here we show that mineral reactions and deformation in amphibolites occurred mainly by coupled dissolution-precipitation and dissolution-precipitation creep at epidote-amphibolite facies conditions, and that fracturing was the most efficient porosity-generating mechanism assisting deformation. Metamorphism and deformation in the amphibolites resulted in the development of a > 500 m thick mylonitic foliation during Caledonian nappe thrusting.

2 | GEOLOGICAL SETTING

The Scandinavian Caledonides developed due to the closure of the Iapetus Ocean in the Ordovician, and the subsequent subduction and continent collision of the Baltica plate below the Laurentia plate in the Silurian to early Devonian (e.g. Gee, Fossen, Henriksen, & Higgins, 2008; Roberts, 2003; Roberts & Gee, 1985; Stephens, 1988). In the Scandinavian Caledonides, tectonic units were transported up to 400 km to the east (Gayer, Rice, Roberts, Townsend, & Welbon, 1987; Gee, 1975; Gee, Juhlin, Pascal, & Robinson, 2010; Rice & Anderson, 2016; Roberts & Gee, 1985) as a result of the collision, creating a nappe stack of several allochthonous units on top of Autochthonous Baltic Shield (Figure 1a,b). After emplacement, the nappe stack was folded into north-trending synforms and antiforms, possibly related to the crustal extension and normal faulting occurring during the latest orogenic phases (Bergman & Sjöström, 1997). By virtue of their deep erosional level, the internal parts of the Scandinavian Caledonides expose middle and lower crustal sections involved in subduction-exhumation history and nappe stacking.

The Scandinavian Caledonides are subdivided, from top to bottom, into an Uppermost Allochthon, an Upper Allochthon, a Middle Allochthon, and a Lower Allochthon based on tectonostratigraphy (Figure 1; Gee & Sturt, 1985; Strand & Kulling, 1972; Strömberg et al., 1984). The Middle Allochthon, the target of this study, includes several basement units and associated metasedimentary rocks representing the outermost Baltica margin and possibly including units derived from an ocean-continent transition zone (e.g. Andréasson, 1994; Gee et al., 2008; Gee, Janák, Majka, Robinson, & van Roermund, 2013; Roberts, 2003; Stephens, 1988). The upper tectonic unit of the Middle Allochthon is the Seve Nappe Complex (SNC; e.g. Sjöström, 1983), which, in the central Scandes, outcrops over a N-S distance of ~1000 km and an W-E distance of ~200 km (Figure 1; Andréasson, 1994).

In the Jämtland region, the SNC can be further subdivided into Lower, Middle and Upper Seve Nappe by the presence of internal thrust sheets (Zachrisson & Sjöstrand, 1990). The Lower Seve Nappe is mainly composed of micaschists, quartzites and metapsammites with gneisses, metabasites and with minor peridotites and serpentinites (Figure 1c). The Middle Seve Nappe is composed of similar lithotypes, but overprinted by a pervasive migmatization. Several parts of the Lower- and Middle Seve preserve evidence of high pressure (HP) to ultrahigh pressure (UHP-) metamorphism (summary in figure 4 of Klonowska, Janák, Majka, Froitzheim, & Kościńska, 2016) spanning from ~1.1 GPa and 600°C up to 4 GPa and 800°C, within the stability field of coesite and diamond (Brueckner & van Roermund, 2004; Gilio, Clos, & van Roermund, 2015; Janák, van Roermund, Majka, & Gee, 2013; Klonowska et al., 2016; Klonowska et al., 2017; Majka et al., 2014; Van Roermund, 1985, 1989). The HP-UHP metamorphism is the manifestation of the Ordovician subduction of the SNC (Brueckner & Van Roermund, 2007; Ladenberger et al., 2013; Root & Corfu, 2012). It is worth noting that to date, no evidence of (U)HP metamorphism has been recorded in the Lower Seve Nappe in the central Jämtland. In the Middle Seve Nappe, the granulite and amphibolite facies metamorphism appears to postdate the HP-UHP stage, and produced partial melting at 442–436 Ma (Ladenberger et al., 2013). A recent study has related the amphibolite facies metamorphic “stage” to the exhumation and lateral extrusion of the SNC (Grimmer, Glodny, Drüppel, Greiling, & Kontny, 2015). In the Lower Seve Nappe, a pervasive amphibolite facies foliation overprints the (U)HP fabric where present; where not present it represents the main metamorphic fabric. In the Åreskutan area, the amphibolite facies metamorphic stage was constrained at 550°C and 0.2 to 0.5 GPa (Arnbom, 1980).

The “Collisional Orogeny in the Scandinavian Caledonides (COSC-1)” borehole (Lorenz et al., 2015; see location in Figure 1b,c) is located in the central Jämtland region, near Åre (Sweden). The drill core provides an almost complete section (recovery rate higher than 99%) through the Lower Seve Nappe. In detail, the core comprises alternating layers of felsic gneisses, calc-silicates and amphibolites displaying narrow (mm-cm) and localized shear zones from the surface down to 1700 m (Hedin et al., 2016). The rocks show strongly deformed fabrics from 1700 m to 2500 m (the end of the core; Lorenz et al., 2015), with the development of mylonitic fabrics. The lowermost portion of the core is composed of strongly deformed metasedimentary rocks. Acoustic televiewer data indicates that the foliation is generally shallow and trends N-S, but there are remarkable exceptions, where the foliation has dips to the E or W with angles $>50^\circ$, related to recumbent folds and boudinage (Wenning et al., 2017).

3 | METHODS

3.1 | Scanning electron microscopy (SEM)

All the SEM analyses were performed on carbon-coated polished thin sections cut perpendicular to the foliation and parallel to the stretching lineation of the sample. Backscattered electron (BSE) and cathodoluminescence (CL) analyses were performed at the Open University (UK), using an FEI Quanta 200 three-dimensional SEM on carbon coated thin sections. Analyses were conducted under high vacuum, using an accelerating voltage of 10 kV, a beam current of 3.3 nA, a working distance of 13 mm, and an electron source provided by a tungsten filament. The panchromatic CL detector used is a Centaurus Deben with a photo multiplier tube (Hamamatsu R316) characterized by sensitivity in the range of 400-1200nm.

Electron backscattered diffraction (EBSD) analyses were conducted with a Jeol-7001FEG SEM at the Electron Microscopy Centre, Plymouth University (UK). EBSD patterns were acquired with a 70° tilted sample geometry, 20 kV accelerating voltage, 18-23 mm working distance and 1.3-1.7 μm step size. Diffraction patterns were automatically indexed using AZtec (Oxford Instruments). The indexing match units used for the analysed phases were “anorthite” (Laue group -1) for albite and oligoclase, and “hornblende” (Laue group 2/m) for tschermakite-ferrotschermakite. Both match units were taken from the American Mineralogist database. Raw maps were processed with HKL Channel 5 (Oxford Instruments), using the noise reduction procedure tested by Prior, Wheeler, Peruzzo, Spiess, and Storey (2002). Wild spikes were removed, and un-indexed points were replaced by the average orientation of the neighbour points. Grains smaller than three times the step size were not considered in the analysis. The mean angular deviation values were 0.3 for amphibole and 0.4-0.6 for plagioclase; the raw indexing rate ranged between 90 and 95%. Crystallographic directions were plotted on pole figures (upper and lower hemisphere of the stereographic projection), with X parallel to the stretching lineation and Z parallel to the pole of the mylonitic foliation. The grain orientation spread maps (GOS maps) were calculated as the average misorientation between every pixel in the grain and the grain’s average orientation.

3.2 | Electron probe micro-analyser (EPMA)

EPMA analyses were conducted at the Open University (UK), using a Cameca SX100 connected to five spectrometers. Wavelength dispersive spectrometers (WDS) were used for both spot analyses and X-ray maps, the latter acquired following the procedure of Lanari et al. (2013). Spot analyses were acquired first for each mineral, before performing the X-ray maps on the same area. Spot analyses were performed with 20 KeV accelerating voltage, 20 nA specimen current and 2 μm beam diameter. Ten oxide compositions were measured, using natural standards: K-feldspar (SiO_2 , Al_2O_3 , K_2O), bustamite (CaO , MnO), hematite (FeO), forsterite (MgO), jadeite (Na_2O), rutile (TiO_2), apatite (P_2O_5). A ZAF matrix correction routine was applied; uncertainty on major element concentrations was $<1\%$. X-ray maps were acquired with 15 KeV accelerating voltage, 100 nA specimen current,

dwel times of 70-100 ms and step size of 5 μm . Ten elements (Si, Ti, Al, Fe, Mn, Mg, Na, Ca, K and P) were measured at the specific wavelength in two series. Intensity X-ray maps were standardized to concentration maps of oxide weight percentage using spot analyses as internal standard. X-ray maps were processed using XMapTools 2.2.1 (Lanari et al., 2014).

3.3 | Geothermobarometry

3.3.1 | Amphibole-plagioclase thermobarometry

Temperature was estimated using the Holland and Blundy (1994) geothermometer, which is based on element exchange between amphibole and plagioclase pairs in equilibrium. The calibration reaction edenite+albite = richterite+anorthite was constrained from experimental and natural data for silica-saturated and silica-rich igneous and metamorphic rocks in the range of 0.1-1.5 GPa and 400-1000 $^{\circ}\text{C}$.

Pressure was estimated using two geobarometers: Bhadra and Bhattacharya (2007) and Anderson and Smith (1995). The former is based on element distribution between amphibole and plagioclase pairs in equilibrium. Experimental data were conducted on silica-saturated assemblages in the P - T range of 0.1-1.5 GPa and 650-950 $^{\circ}\text{C}$, and on the reaction tremolite+tschermakite+2 albite = 2 pargasite+8 quartz. The latter is based on the increase of Al in hornblende with increasing pressure and is calibrated on experimental data at 675 and 760 $^{\circ}\text{C}$, accounting for the effects of temperature and f_{O_2} . Pressure and temperature were calculated using the Plagioclase–Hornblende Thermobarometry spreadsheet (Anderson, Barth, Wooden, & Mazdab, 2008) and the spreadsheet of Wallis, Phillips, and Lloyd (2014) (the latter was used to derive pressure from the calibration of Bhadra & Bhattacharya, 2007).

3.3.2 | Chlorite+Quartz+H₂O thermometry

Chlorite+Quartz+H₂O thermometry was performed using the program CHLMICA_{EQUI} (Lanari, 2012). The crystallization temperature of chlorite and the $X_{\text{Fe}^{3+}}$ were computed at a fixed pressure of 0.7 GPa in the range of 100 to 550 $^{\circ}\text{C}$ from the convergence of four equilibria involving five chlorite end-members, quartz and H₂O (Lanari et al., 2012; Vidal, Lanari, Munoz, Bourdelle, & De Andrade, 2016) using standard state properties and solid solution models of Vidal, Parra, and Vieillard (2005; 2006).

4 | RESULTS

4.1 | Petrography and microstructure

In the middle and lower portions of the COSC-1 borehole (~1500-2300 m depth), amphibolites show a mylonitic foliation. The studied sample (International Geological Sample Number: ICDP5054EX8E601) was extracted from a depth of 2206.97 m from the surface and is similar to several amphibolite samples present between ~1600 and ~2300 m depth. In this sample the mylonitic foliation is subhorizontal, it wraps around plagioclase porphyrocrysts and is defined by amphibole, plagioclase (with smaller grain size, details in the following), chlorite, quartz, epidote and ilmenite (Figure 2). Quartz and calcite occur mainly in veins subparallel to the mylonitic foliation or as fine grains dispersed in the mylonitic foliation, typically along the phase boundaries between plagioclase and amphibole.

Plagioclase is present as zoned porphyrocrysts (up to 0.5-1 cm in size) wrapped by the mylonitic foliation, and as finer (up to hundreds of μm in size) albite/oligoclase grains elongated parallel to the mylonitic foliation (aspect ratios up to ~5; mean ~2). Plagioclase porphyrocrysts have albite cores that appear turbid due to abundant fine-grained (up to 30 μm in size) inclusions of ilmenite, rutile and epidote. Ilmenite crystals are also included with bigger grain size (100 μm in size); quartz is present as inclusions with variable grain size (tens to hundreds of μm in size; Figures 3 and 4). The inclusions locally define a rotated internal foliation (upper plagioclase porphyrocryst in Figure 3a). These cores are porphyroclastic, and are cut by fracture systems and some are dismembered parallel to the foliation (see details in section 4.2). The cores are always surrounded by

albite/oligoclase rims. Pores are evident in the albite/oligoclase rims: they are few microns in size and occur in trails parallel to fracture systems that dissect the plagioclase core (Figure 4). Several mineral inclusions also occur along such trails, ranging from a few microns to tens of microns in size. These are muscovite, epidote and calcite, with rare Ba-rich muscovite (Figure 4). Such inclusions confer a turbid aspect to plagioclase rim in plane-polarized light micrographs (Figure 3a; Table 1).

Amphibole is pleochroic, with absorption colours ranging from light brown to dark green-blue; in some bigger crystals absorption colours highlight a paler core and a darker rim. Amphibole displays the C-axis parallel to the stretching lineation and a maximum grain size of >1 mm. Chlorite has a pleochroism varying from light yellow to light green, a negative optical sign and grain size similar to the amphibole. Asymmetric pressure shadows around plagioclase porphyroclasts indicate both dextral and sinistral sense of shear. In these pressure shadows amphibole, albite/oligoclase grains and chlorite crystallize intergrown and elongated parallel to the mylonitic foliation. C' planes display a dominant sinistral sense of shear and are defined by the same minerals found along the mylonitic foliation (Figures 2 and 3a-b). Opaque minerals include mostly ilmenite, up to 1 mm in size, with minor magnetite and pyrite. Ilmenite crystals are elongate and lie parallel to the mylonitic foliation.

4.2 | Microstructure and chemistry of plagioclase

BSE images highlight two plagioclase generations: dark cores with an albitic composition (PI1) are surrounded by brighter plagioclase rims with higher anorthite content (PI2 and PI3, as defined based on chemistry in the next paragraph; Figures 3c and 4). Furthermore, the cores are cut by fractures filled with plagioclase with the same composition as the plagioclase rims. The distinction of these plagioclase generations is more evident in the CL images, where plagioclase cores appear moderately luminescent and are surrounded by bright plagioclase rims (Figure 3d). The fractures dissecting the cores are as bright as the plagioclase rims. The plagioclase cores (PI1) are locally fragmented and display lobate edges and embayments that are typically surrounded by bright plagioclase (Figures 3d, 7a and 8b). In some areas, the plagioclase rims can be further subdivided into two generations based on the brightness of their CL response: a brighter plagioclase generally surrounded by a darker one (PI2 and PI3, respectively).

Compositional maps of plagioclase display a perfect match with the CL images (Figure 3e). The maps highlight three plagioclase compositions, numbered from the older to the younger: PI1 (XAn 0-0.05), PI2 (XAn 0.13-0.25), PI3 (XAn 0.05-0.13; Figures 5a and 7b; Table 2). The plagioclase core (PI1) has an albite composition and is overgrown by the two albite/oligoclase rims (PI2 and PI3). PI2 is present only locally and is overgrown by PI3, as shown in the top right corner of Figure 3e. Furthermore, PI3 seals the fractures inside PI1. PI1 forms porphyroclasts wrapped by the mylonitic foliation, whereas PI2 and PI3 occur in the pressure shadows of PI1.

4.3 | Microstructure and chemistry of amphibole and chlorite

Compositional maps of amphibole crystals display corroded cores, higher in Mg# ($Mg\# = Mg/(Fe^{2+} + Mg)$; Amp1: Mg# 0.5-0.44, Si apfu 7-6.5), and rims, lower in Mg# (Amp2: Mg# 0.44-0.36, Si apfu 6.5-6.1; Figures 3f and 5b; Table 2). Based on the classification of Leake et al. (1997) the Amp1 is at the compositional boundary between tschermakite-ferrotschermakite-magnesioghornblende-ferrohornblende; Amp2 is a ferrotschermakite (Figure 5c). There are local exceptions to this zoning pattern, in which the two peripheral areas have higher Mg# (Figure 9c). Amp2 and PI3 grains displaying mutual intergrowths and elongation parallel to the foliation (Figure 3 c-f)

Chlorite is characterized by a homogeneous Mg# (Mg# 0.59-0.56, Chl1), except along grain boundaries and the C' planes, where some lower values are visible (Mg# 0.55-0.52, Chl2; Figure 5c; Table 3). Chl1 grains occur as intergrown with PI3 and Amp2 along the mylonitic.

4.4 | Amp-Pl thermobarometry

Thermometric estimates for the Pl1 and Amp1 pair yield 400°C; thermobarometric estimates for the Pl2 and Amp1 pair and the Amp2 and Pl3 pair yield 615°C and 0.97 GPa and 605°C and 0.74 GPa respectively ($\pm 50^\circ\text{C}$ ± 0.2 GPa, Table 4; see Section 5.1 for discussion on the plagioclase and amphibole growth zones that we consider to be in equilibrium).

4.5 | Chlorite+Quartz+H₂O thermometry

Chlorite+Quartz+H₂O thermometry was performed on the two different chlorite groups, Chl1 and Chl2 (Figure 5c), at a fixed pressure of 0.7 GPa. The Chl1 displays two peaks in the T-frequency diagram (Figure 6a): one close to the temperature limit of the thermometer (550-450°C) and one at lower temperature (400°C-250°C). Chl2 yields a range of 200-350°C, with a peak at ~250°C (Figure 6b), with only one grain yielding a higher value (~500°C).

4.6 | EBSD analysis

Figures 7 and 8 show the results of EBSD analysis of two microstructural domains (see Figures 2 and 3 for the location of EBSD maps): domain 1 includes a plagioclase porphyrocryst with a core of Pl1 composition rimmed by Pl2 and Pl3 compositions. The porphyrocryst Pl1 is cut by a network of intracrystalline microfractures oriented NW-SE and filled with Pl2-Pl3. Domain 1 also includes clusters of amphibole and plagioclase grains around the plagioclase porphyrocryst (Figure 7). Domain 2 contains an aggregate of amphibole grains, mostly elongate parallel to the foliation, and several grains of plagioclase showing a core-and-rim zoning in CL images (Figure 8).

The comparison between EBSD maps, CL images and compositional maps shows that the Pl1 porphyrocrysts, which EBSD identifies as one individual grain (i.e. it does not contain high-angle boundaries with misorientation $> 10^\circ$), actually include areas with Pl2 and Pl3 compositions, which maintain the original crystal shape and crystallographic orientation of Pl1 (Figures 7 and 8). The internal distortion of the compositionally zoned porphyrocrysts, as evaluated with the GOS, is rather low (GOS values lower than 2° : Figures 7c and 8e). Low-angle boundaries (misorientations 2 - 10°) are preferentially distributed along the microfractures. The analysis of local misorientations within Pl1 cores indicates that Pl2 and Pl3 areas have misorientations of up to 2° with respect to the Pl1 cores (Figure 7d). Higher misorientations (up to 3°) are found in the plagioclase porphyrocryst of the domain 2 (Figure 8d).

In domain 1, the compositionally zoned plagioclase porphyrocryst is surrounded by Pl2-Pl3 grains that range in size between 30 and 200 μm , delimited by high-angle boundaries with misorientation $> 10^\circ$ from the porphyrocryst. The Pl2 and Pl3 grains have mean GOS values lower than 1° , with one maximum value of 4° .

Amphibole generally shows GOS values lower than 2° , with a few maxima of up to 7° (Figures 7e, 8g, and 9d). Misorientations progressively increase towards fractures perpendicular to the crystal elongation and, locally, towards very few low angle boundaries oriented subparallel to the crystal elongation (Figures 7f, 8h, and 9f). The misorientation profile in Figure 9e highlights a jump in misorientation of up to 7° across the low angle boundary.

The crystallographic orientation of the new grains of Pl2 and Pl3 displays a variable degree of overlap with the one of the Pl1 core that they overgrow (Figures 10a,b and 11a,b). In some cases, all the new grains inherit the crystallographic orientation of the Pl1 core (Figure 10a,b), whereas in other cases, the overlap is more limited and the new grains show a significant dispersion of crystallographic directions with respect to the Pl1 cores (Figure 11). The crystallographic inheritance is more evident if we consider the crystallographic orientation of the Pl2-Pl3 grains in direct contact with the Pl1 core (Figures 10a and 11b). The Pl2-Pl3 grains dispersed in the mylonitic matrix show a wide range of crystallographic orientations, which do not necessarily overlap with those of the Pl1 cores included in the map (Figures 10b and 11a). EBSD analysis also shows that the most common

fracture set in the Pl1 porphyroclasts is parallel to the (001) plane, which is a perfect cleavage plane in plagioclase (Figure 11a).

Amphibole has a strong CPO, with the (100) and [001] subparallel to the foliation and to the stretching lineation, respectively (Figures 10c and 11c). The misorientation angle distribution of amphibole displays the strongest peaks between 2 and 25° and around 50 and 180°, with higher values for the correlated pairs (Figure 11d). The misorientation axes of amphibole, plotted in crystal coordinates, show maxima around the c-axis for misorientations up to 30°, which, in sample coordinates, is oriented subparallel to the stretching lineation of the mylonite (Figure 11d).

5 | DISCUSSION

5.1 | *P-T* conditions of metamorphism and deformation

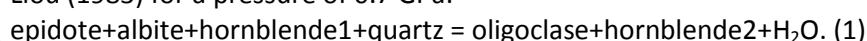
The Anderson and Smith (1995) geobarometer calibration was based on rocks that equilibrated in the presence of melt. There is no evidence of melt in our sample, therefore we favour the pressure results from Bhadra and Bhattacharya (2007; Table 4). However, both results, are kept as the Plagioclase–Hornblende Thermobarometry spreadsheet (Anderson et al., 2008) that were used to compute *P-T* utilises a convergence between the results of Anderson and Smith (1995) geobarometer and Holland and Blundy (1994) geothermometer. As a test, the Bhadra and Bhattacharya (2007) pressure results were used as input for the Holland and Blundy (1994) geothermometer and coincident temperature results were obtained, within error.

The oldest metamorphic stage preserved in the sample is represented by the albite cores (Pl1) with their oriented inclusions of epidote, ilmenite and rutile. In particular, rutile inclusions suggest relatively high pressure, but the coexistence with albite crystals would constrain the maximum pressure of this metamorphic stage below the albite breakdown reaction (albite = jadeite+quartz; Newton & Smith, 1967). However, the exact conditions of this first metamorphic stage were not constrained in this study.

The microstructural relationships between Pl1 and Amp1 are equivocal, therefore it is difficult to prove that they grew in equilibrium. Their compositions suggest that had they grown in equilibrium, they would have crystallized at 400°C (Table 4). These results, however, are far away from the lower limits of the calibration of Bhadra and Bhattacharya (2007; 650–950°C) and Anderson and Smith (1995; 675–760 °C): for this reason, pressures were not computed for the Amp1-Pl1 pairs. Furthermore, Pl1 is out of the compositional range of the Bhadra and Bhattacharya (2007) equilibration (Table 10 of that contribution).

Within uncertainty, the temperature results of Amp1-Pl2 and Amp2-Pl3 pairs lie just within the lower limits of the two calibrations. The *P-T* estimates from the Amp1-Pl2 and Amp2-Pl3 pairs are coincident within error (± 0.2 GPa and ± 50 °C). This is due to the subtle chemical differences existing between these two generations. Thermobarometric calculations suggest that Pl2 may have grown synchronously with Amp1 at 615°C and 0.97 GPa. The crystallization of Pl2 marks the first stage of the mylonitic foliation development, as evidenced by the presence of Pl2 in the pressure shadows of Pl1 (Figures 3, 5a and 7). The mylonitic foliation continued to develop under conditions of $\sim 600^\circ\text{C}$ and 0.75 GPa (Amp2-Pl3 pair), as supported by the microtextural observation of Amp2, Pl3 and Chl1 intergrowths within the Pl1 pressure shadows (Section 4.1). This temperature result is coincident, within error, with the Chlorite+Quartz+H₂O thermometry results for Chl1 (550°C; higher temperature peak in Figure 6a).

The XAn increase from Pl1 to Pl2 and Pl3 could reflect the following reaction from Apter and Liou (1983) for a pressure of 0.7 GPa:



The abundant epidote inclusions in Pl1 and its scarcity and corroded aspect in the matrix of the sample would support this hypothesis. Pl2 likely crystallized at $>600^\circ\text{C}$ in the (High-T) epidote-amphibolite facies field (Apter & Liou, 1983; Liou, Kuniyoshi, & Ito, 1974; Miyashiro, 1968; Winkler, 1980), and Pl3 at lower temperatures, as the associated Amp2 and Chl1 limit the maximum

temperatures to 550-600°C (Figures 5 and 6a). A final retrograde stage is recorded by the Chl2 compositions suggesting a range of 350-200°C (using the Chlorite+Quartz+H₂O thermometry, Figure 6b), and by the overprinted Chl1 values yielding the low-*T* peak of Figure 6a. Indeed, Chl2 appears to be associated with the development of *C'* shear bands overprinting the mylonitic foliation.

5.2 | The origin of luminescence in plagioclase

BSE and CL images provide important insight into feldspar textures (e.g. Lee, Parsons, Edwards, & Martin, 2007; Parsons & Lee, 2009; Parsons, Steele, Lee, & Magee, 2008). Plagioclase luminescence has been related to many causes (summarized in Götze, 2012): the Mn²⁺, Ti, Fe³⁺ content (Götze, Habermann, Kempe, Neuser, & Richter, 1999; Mariano & King, 1975), trace and REE elements (Götze, Habermann, Neuser, & Richter, 1999; Mariano & King, 1975), lattice defects (e.g. Al-O-Al bridge; Finch & Klein, 1999) and/or mineral inclusions (Smith & Stenstrom, 1965). The CL signal is most commonly linked to Ti concentrations (Lee et al., 2007; Parsons et al., 2008), with a contribution from Fe (Lee et al., 2007). Furthermore, Parsons et al. (2008) has noted that CL emissions appear to be linked to Ca zoning, but they did not find a direct link between Ca concentration (or other trace element concentrations) and CL intensity.

In our samples, TiO₂ appears uniform across all Pl generations (at 0.01wt%; Table 2). This is also the case for the MnO, with a scatter between 0.002 and 0.006 wt%. The FeO (Fe total) in Pl1 and Pl2 is the same (0.03 wt%; Table 2), but increases in Pl3 (0.06 wt%; Table 2). The CL signal in our samples appears to be related to the Ca/Na ratio (with maybe some contribution from Fe): the higher the ratio the brighter the growth zone, as visible from the perfect match between the SEM-CL and EPMA compositional maps (Figures 3 and 7), even though we cannot rule out a contribution from trace and REE elements or lattice defects. Luminescence induced by calcite inclusions in Pl2 and 3 can be excluded, as the calcite veins in the sample do not luminesce.

5.3 | Replacement reactions by coupled dissolution-precipitation and deformation by dissolution-precipitation creep in plagioclase and amphibole

Our analysis highlights a strong correlation between CL images and both BSE images and EPMA compositional maps of plagioclase. Textural and chemical features similar to those reported in this study are recognised in several amphibolites present over > 500 m of the COSC-1 core (from ~1600 to ~2300 m depth), implying that the deformation mechanisms and the mineral replacement reactions discussed below are important for the development of the middle to lower crustal thrusts and associated tectonic transport during Caledonian nappe stacking.

The plagioclase porphyrocrysts deformation history is summarized in Figure 12a. During the first stage Pl1 grew including a foliation defined by quartz, epidote, ilmenite and rutile. Subsequently, fractures developed along the (001) cleavage planes (Ague, 1988; Brander et al., 2012; Brown & Macaudière, 1984; McLaren & Pryer, 2001) enhanced fluid infiltration that triggered replacement reactions occurring via coupled dissolution of Pl1 and precipitation of Pl2 (Brander et al., 2012; Marti, Stünitz, Heilbronner, Plümper, & Drury, 2017) in equilibrium with the changed *P-T* conditions of 0.9 GPa and 615° C. These replacement processes continued precipitating Pl3, which rimmed Pl1 and Pl2 and sealed the fractures in Pl1. The slightly different chemistry of Pl3 compared to Pl2 and the microstructural observation that Pl3 overgrows Pl2 suggest that these two growth zones were closely related in time or crystallization reaction (Section 4.2).

The growth zones of Pl2 and Pl3 inherit the crystallographic orientation of the Pl1 cores, with maximum misorientation of 5° (Figure 7c,d). Thus, the precipitation of Pl2 and Pl3 on Pl1 is an example of pseudomorphic and topotaxial growth, as often observed during coupled dissolution-precipitation processes (Engvik et al., 2008; Hövelmann, Putnis, Geisler, Schmidt, & Golla-Schindler, 2010; Plümper et al., 2017; Putnis & Putnis, 2007; Spruzeniece, Piazzolo, & Maynard-Casely, 2017). The small (generally < 2°) and only local difference in crystallographic orientation between Pl1 and

PI2-PI3 presumably results from the slightly different unit cell parameters between albite and oligoclase. The few low angle boundaries associated with PI2-PI3 growth zones are typically found along intracrystalline fractures (Figure 7d), and we interpret them as evidence of slightly rotated fractured fragments of PI1 that re-equilibrated to PI2-PI3 compositions via coupled dissolution-precipitation processes. Pore trails occur in the plagioclase porphyrocrysts parallel to the two fracture systems, together with several micrometric mineral inclusions resulting in a turbid aspect of the plagioclase (Figures 3a,b and 4). Those trails probably represented the main pathways of fluid circulation during coupled PI1 dissolution and PI2 and PI3 precipitation. These mineral inclusions may represent the signature of transient porosity during plagioclase replacement reactions (e.g. Plümper et al., 2017; Plümper & Putnis, 2009; Putnis, 2015; Walker, Lee, & Parsons, 1995).

Crystallographic continuity indicative of epitaxial overgrowth is also observed between plagioclase porphyrocrysts and PI2 and PI3 grains around them, but to different extents (compare Figure 10a with Figure 11b). Thus, the crystallographic orientation of new PI2 and PI3 grains may be inherited from the PI1 parent grain due to epitaxy, as described for several minerals deforming by dissolution-precipitation creep at different crustal levels (Engvik et al., 2008; Imon et al., 2002; Imon et al., 2004; Jiang, Prior, & Wheeler, 2000; Mukai et al., 2014; Spruzeniece et al., 2017; Wassmann & Stöckhert, 2012; Wassmann et al., 2011). The crystallographic continuity seems to decrease away from the plagioclase porphyrocrysts (Figures 10b and 11a), presumably reflecting the heterogeneous nucleation of PI2 and PI3 neoblasts in the surrounding matrix together with Amp2 and Chl1. Additionally, these neoblasts may have also undergone grain-boundary sliding during deformation, given their fine grain size, which can further disperse their inherited crystallographic orientation (Okudaira et al., 2017).

Thus, we conclude that metamorphism of plagioclase at $\sim 600^\circ\text{C}$ and 0.75-0.9 GPa occurred by coupled dissolution-precipitation processes with pseudomorphic and topotaxial replacement of PI1 by PI2 and PI3, and deformation was accommodated by dissolution-precipitation creep with nucleation of PI2-PI3 grains around the plagioclase porphyrocrysts (epitaxial) and in the surrounding matrix. It is worth noting that the replacement of PI1 porphyroclasts by coupled dissolution-precipitation processes generally occurred concentrically (Figure 7). Consequently, at least part of this replacement process outlasted the deformation. The similar chemistry of PI3 replacing PI1 and the PI3 neoblasts in the surrounding matrix suggest that there was no major change in metamorphic conditions throughout the timing of growth of PI3.

No significant contribution of crystal plasticity was observed, although deformation occurred at *P-T* conditions at which crystal plasticity in plagioclase is expected to occur (e.g. Gerald & Stünitz, 1993; Pearce, Wheeler, & Prior, 2011). The porosity necessary to maintain fluid transport during coupled dissolution-precipitation was generated mostly by fracturing, as shown by the common occurrence of PI2-PI3 growth zones along fractures parallel to the (001) perfect cleavage planes. Finally, the sharp chemical transition (across $\sim 1\text{-}5\ \mu\text{m}$) between all the plagioclase generations, visible from the EPMA and CL maps (Figures 3 and 7), suggest that chemical equilibration did not occur by solid-state diffusion (e.g. Hövelmann et al., 2010).

The textural features of amphibole suggest a similar deformation history to plagioclase (Figure 12b). Amp1 (high Mg#) grains are preserved mostly as relict cores and display embayments, lobate edges and truncated chemical zoning patterns (Figures 3f and 9c; Bukovská, Wirth, & Morales, 2015; Gratier et al., 2013; Hyppolito, García-Casco, Juliani, Meira, & Hall, 2014; Passchier & Trouw, 1996; Rutter, 1983; Stokes et al., 2012; Wassmann & Stöckhert, 2013; Wintsch & Yi, 2002). These textural features suggest that Amp1 underwent coupled dissolution and Amp2 precipitated on Amp1. As for plagioclase, the growth of Amp2 on Amp1 was pseudomorphic and topotaxial (Figure 9d-f). Amp2 grew also as smaller neoblasts (maximum few hundreds of μm in size), elongated parallel to the mylonitic foliation and preferentially elongated parallel to their *c*-axis, due to dissolution-precipitation creep. These crystals do not display Amp1 cores in the compositional maps (Figures 3f and 5b).

The CPO and shape-preferred orientation of the amphibole can be acquired via different mechanisms: dissolution-precipitation creep (Bons & den Brok, 2000; Imon et al., 2004; Pearce, Wheeler, & Prior, 2011), oriented grain growth and passive rotation after growth (Berger & Stünitz, 1996; Kanagawa, Shimano, & Hiroi, 2008) and/or diffusion creep (Getsinger & Hirth, 2014). In the studied sample the CPO displayed by Amp2 is mostly inherited due to the pseudomorphic and toptaxial growth on Amp1. The small misorientations ($< 3^\circ$) evident in the EBSD map (Figure 9f) are attributed to fractures that developed perpendicular to the crystal elongation (Figure 9a). Some amphibole crystals display more complex zoning (e.g. central crystal in Figure 9c), probably due to a preferential replacement of the central part of the crystal (e.g. Hyppolito et al., 2014). The CPO of Amp1 grains was presumably formed via oriented grain growth during an earlier deformation event. Moreover, as presented in section 4.6, the misorientation axes of amphibole show maxima around the c-axis, which is oriented subparallel to the stretching lineation of the mylonite (Figure 11d). This geometry is not consistent with dislocation creep on the prism $\langle c \rangle$ slips system of amphibole, as the misorientation axis cannot coincide with the Burgers vector (e.g. Kruse, Stünitz, & Kunze, 2001; Lloyd, Farmer, & Mainprice, 1997). Instead, we interpret the cluster of misorientation axes around $\langle c \rangle$ as evidence of toptaxial growth of elongated amphibole grains that preferentially share their c-axis. As the data come from all the grains included in the map (and not only from the rims of Amp2), we think that oriented growth was the dominant deformation mechanisms of amphibole throughout the deformation history.

In the studied sample amphibole, like plagioclase, shows no evidence of deformation via crystal plasticity, such as high intracrystalline misorientations, misorientation bands, subgrains. Instead it appears to have deformed by fracturing and coupled dissolution-precipitation, as also suggested in other studies (Berger & Stünitz, 1996; Brodie & Rutter, 1985; Lafrance & Vernon, 1993; Nyman, Law, & Smelik, 1992; Pearce et al., 2011). Crystal plasticity is potentially a more effective deformation mechanism at higher temperatures (e.g. Skrotzki, 1992).

It is worth noting that the synkinematic reaction that produced Pl2-Pl3 and Amp2 (reaction 1) could have been a dehydration reaction. If this was the case, the aqueous fluid necessary to sustain coupled dissolution-precipitation processes did not necessarily infiltrate from an external source, but may have been released internally. The role of dehydration reactions in the rheological evolution of crustal rocks has received little attention so far, as reaction weakening is commonly associated with hydration reactions during retrogression (e.g. Gueydan, Leroy, Jolivet, & Agard, 2003). However, dehydration reactions that release fluids at grain boundaries can also potentially result in weakening and strain localization during burial and nappe stacking, if the released fluids facilitate the activation of coupled dissolution-precipitation creep and of diffusion creep.

6 | CONCLUSIONS

Middle to lower crustal mylonites from the COSC-1 drill core (Lower Seve Nappe) were investigated with EPMA compositional maps, CL images and EBSD maps to constrain the mechanism(s) responsible for their formation. The data suggest that fracturing, coupled dissolution-precipitation and dissolution-precipitation creep were responsible for the development of the mylonitic fabric in amphibolites at conditions of $\sim 600^\circ\text{C}$, 0.75-0.97 GPa, in the epidote-amphibolite facies, over a thickness of > 500 m. No evidence of deformation via crystal plasticity is present in either plagioclase or amphibole in the analysed sample, even though deformation occurred at P - T conditions at which plagioclase is expected to deform by dislocation creep. The presence of H_2O -rich fluid at the grain boundaries appears to have enhanced replacement reactions and facilitated dissolution and precipitation processes, which in turn considerably decreased the strength of this middle to lower crustal shear zone. Importantly, replacement reactions of plagioclase only occurred by coupled dissolution-precipitation at grain boundaries and along fractures, and were otherwise sluggish.

Our study shows that crystallographic preferred orientation in plagioclase and amphibole can be inherited from parental grains due to pseudomorphic and toptaxial growth during coupled

dissolution-precipitation during deformation. Thus, care must be taken when considering CPOs in deformed rocks as evidence of deformation by dislocation creep.

The development of a mylonitic fabric by coupled dissolution-precipitation and dissolution-precipitation creep in amphibolites over a thickness > 500 in the Lower Seve Nappe suggests that the strength of amphibolites can be significantly low in the presence of grain-boundary aqueous fluid during nappe thrusting in the middle to lower crust.

ACKNOWLEDGEMENTS

S. Hammond and D. Johnson are warmly thanked for the help with EPMA and SEM analyses, respectively. The staff at Plymouth University Electron Microscopy Centre is acknowledged for the support during EBSD analysis. B. Almqvist is acknowledged for his support in acquiring the sample. We acknowledge constructive comments and suggestions from M.A. Pearce, R. Wintsch and two anonymous referees that improved the quality of the manuscript. We are grateful to M. Brown for editorial handling. This work was funded by an Early Postdoc.Mobility funding scheme (project number: P2BEP2_168722) granted by Swiss National Science Foundation. LM acknowledges financial support from a FP7 Marie Curie Career Integration Grant (grant agreement PCIG13-GA-2013-618289).

REFERENCES

- Ague, D. M. (1988). Universal stage measurements and transmission electron microscope observations of fractured plagioclase. *Journal of Structural Geology*, 10(7), 701-705.
- Anderson, J. L., Barth, A. P., Wooden, J. L., & Mazdab, F. (2008). Thermometers and thermobarometers in granitic systems. *Reviews in Mineralogy and Geochemistry*, 69(1), 121-142.
- Anderson, J. L., & Smith, D. R. (1995). The effects of temperature and fO₂ on the Al-in-hornblende barometer. *American Mineralogist*, 80(5-6), 549-559.
- Andréasson, P. (1994). The Baltoscandian margin in Neoproterozoic-early Palaeozoic times. Some constraints on terrane derivation and accretion in the Arctic Scandinavian Caledonides. *Tectonophysics*, 231(1-3), 1-32.
- Apted, M. J., & Liou, J. (1983). Phase relations among greenschist, epidote-amphibolite, and amphibolite in a basaltic system. *American Journal of Science*, 283, 328-354.
- Arnbom, J.-O. (1980). Metamorphism of the Seve Nappes at Åreskutan, Swedish Caledonides. *Geologiska Föreningen i Stockholm Förhandlingar*, 102(4), 359-371. doi:10.1080/11035898009454493
- Berger, A., & Stünitz, H. (1996). Deformation mechanisms and reaction of hornblende: examples from the Bergell tonalite (Central Alps). *Tectonophysics*, 257(2), 149-174.
- Bergman, S., & Sjöström, H. (1997). Accretion and lateral extension in an orogenic wedge: evidence from a segment of the Seve-Koili terrane boundary, central Scandinavian Caledonides. *Journal of Structural Geology*, 19(8), 1073-1091. doi:http://dx.doi.org/10.1016/S0191-8141(97)00028-X
- Bhadra, S., & Bhattacharya, A. (2007). The barometer tremolite+ tschermakite+ 2 albite= 2 pargasite+ 8 quartz: Constraints from experimental data at unit silica activity, with application to garnet-free natural assemblages. *American Mineralogist*, 92(4), 491-502.
- Bons, P. D., & den Brok, B. (2000). Crystallographic preferred orientation development by dissolution-precipitation creep. *Journal of Structural Geology*, 22(11), 1713-1722.
- Brander, L., Svahnberg, H., & Piazzolo, S. (2012). Brittle-plastic deformation in initially dry rocks at fluid-present conditions: transient behaviour of feldspar at mid-crustal levels. *Contributions to Mineralogy and Petrology*, 163(3), 403-425.

- Brodie, K., & Rutter, E. (1985). On the relationship between deformation and metamorphism, with special reference to the behavior of basic rocks. In *Metamorphic reactions* (pp. 138-179): Springer.
- Brown, W. L., & Macaudière, J. (1984). Microfracturing in relation to atomic structure of plagioclase from a deformed meta-anorthosite. *Journal of Structural Geology*, 6(5), 579-586.
- Brueckner, H. K., & van Roermund, H. L. (2004). Dunk tectonics: a multiple subduction/eduction model for the evolution of the Scandinavian Caledonides. *Tectonics*, 23(2).
- Brueckner, H. K., & Van Roermund, H. L. (2007). Concurrent HP metamorphism on both margins of Iapetus: Ordovician ages for eclogites and garnet pyroxenites from the Seve Nappe Complex, Swedish Caledonides. *Journal of the Geological Society*, 164(1), 117-128.
- Bukovská, Z., Wirth, R., & Morales, L. F. (2015). Pressure solution in rocks: focused ion beam/transmission electron microscopy study on orthogneiss from South Armorican Shear Zone, France. *Contributions to Mineralogy and Petrology*, 170(3), 31.
- Bürgmann, R., & Dresen, G. (2008). Rheology of the lower crust and upper mantle: Evidence from rock mechanics, geodesy, and field observations. *Annual Review of Earth and Planetary Sciences*, 36.
- Carmichael, D. M. (1969). On the mechanism of prograde metamorphic reactions in quartz-bearing pelitic rocks. *Contributions to Mineralogy and Petrology*, 20(3), 244-267.
- Engvik, A. K., Putnis, A., Gerald, J. D. F., & Austrheim, H. (2008). Albitization of granitic rocks: the mechanism of replacement of oligoclase by albite. *The Canadian Mineralogist*, 46(6), 1401-1415.
- Finch, A. A., & Klein, J. (1999). The causes and petrological significance of cathodoluminescence emissions from alkali feldspars. *Contributions to Mineralogy and Petrology*, 135(2-3), 234-243.
- Fusseis, F., & Handy, M. (2008). Micromechanisms of shear zone propagation at the brittle–viscous transition. *Journal of Structural Geology*, 30(10), 1242-1253.
- Fusseis, F., Regenauer-Lieb, K., Liu, J., Hough, R., & De Carlo, F. (2009). Creep cavitation can establish a dynamic granular fluid pump in ductile shear zones. *Nature*, 459(7249), 974-977.
- Gayer, R., Rice, A., Roberts, D., Townsend, C., & Welbon, A. (1987). Restoration of the Caledonian Baltoscandian margin from balanced cross-sections: the problem of excess continental crust. *Transactions of the Royal Society of Edinburgh: Earth Sciences*, 78(03), 197-217.
- Gee, D. (1975). A tectonic model for the central part of the Scandinavian Caledonides. *American Journal of Science*, 275(A), 468-515.
- Gee, D., Fossen, H., Henriksen, N., & Higgins, A. K. (2008). From the early Paleozoic platforms of Baltica and Laurentia to the Caledonide Orogen of Scandinavia and Greenland. *Episodes*, 31(1), 44-51.
- Gee, D., Janák, M., Majka, J., Robinson, P., & van Roermund, H. (2013). Subduction along and within the Baltoscandian margin during closing of the Iapetus Ocean and Baltica-Laurentia collision. *Lithosphere*, 5(2), 169-178.
- Gee, D., Juhlin, C., Pascal, C., & Robinson, P. (2010). Collisional orogeny in the Scandinavian Caledonides (COSC). *Gff*, 132(1), 29-44.
- Gee, D., & Sturt, B. (1985). *The Caledonide orogen: Scandinavia and related areas* (Vol. 2): Wiley.
- Gerald, J. F., & Stünitz, H. (1993). Deformation of granitoids at low metamorphic grade. I: Reactions and grain size reduction. *Tectonophysics*, 221(3), 269-297.
- Getsinger, A., & Hirth, G. (2014). Amphibole fabric formation during diffusion creep and the rheology of shear zones. *Geology*, 42(6), 535-538.
- Gilio, M., Clos, F., & van Roermund, H. L. (2015). The Friningen Garnet Peridotite (central Swedish Caledonides). A good example of the characteristic PTt path of a cold mantle wedge garnet peridotite. *Lithos*, 230, 1-16.
- Gilotti, J. A. (1989). Reaction progress during mylonitization of basaltic dikes along the Särö thrust, Swedish Caledonides. *Contributions to Mineralogy and Petrology*, 101(1), 30-45.

- Giuntoli, F., Lanari, P., & Engi, M. (2018). Deeply subducted continental fragments – Part 1: Fracturing, dissolution–precipitation, and diffusion processes recorded by garnet textures of the central Sesia Zone (western Italian Alps). *Solid Earth*, 9(1), 167-189. doi:10.5194/se-9-167-2018
- Götze, J. (2012). Application of cathodoluminescence microscopy and spectroscopy in geosciences. *Microscopy and Microanalysis*, 18(06), 1270-1284.
- Götze, J., Habermann, D., Kempe, U., Neuser, R. D., & Richter, D. K. (1999). Cathodoluminescence microscopy and spectroscopy of plagioclases from lunar soil. *American Mineralogist*, 84(7-8), 1027-1032.
- Götze, J., Habermann, D., Neuser, R. D., & Richter, D. K. (1999). High-resolution spectrometric analysis of rare earth elements-activated cathodoluminescence in feldspar minerals. *Chemical Geology*, 153(1), 81-91.
- Gratier, J.-P., Dysthe, D. K., & Renard, F. (2013). The role of pressure solution creep in the ductility of the Earth's upper crust. *Advances in Geophysics*, 54, 47-179.
- Grimmer, J. C., Glodny, J., Drüppel, K., Greiling, R. O., & Kontny, A. (2015). Early-to mid-Silurian extrusion wedge tectonics in the central Scandinavian Caledonides. *Geology*, 43(4), 347-350.
- Gueydan, F., Leroy, Y. M., Jolivet, L., & Agard, P. (2003). Analysis of continental midcrustal strain localization induced by microfracturing and reaction-softening. *Journal of Geophysical Research: Solid Earth*, 108(B2).
- Hedin, P., Almqvist, B., Berthet, T., Juhlin, C., Buske, S., Simon, H., . . . Alm, P.-G. (2016). 3D reflection seismic imaging at the 2.5 km deep COSC-1 scientific borehole, central Scandinavian Caledonides. *Tectonophysics*, 689, 40-55.
- Holland, T., & Blundy, J. (1994). Non-ideal interactions in calcic amphiboles and their bearing on amphibole-plagioclase thermometry. *Contributions to Mineralogy and Petrology*, 116(4), 433-447.
- Hövelmann, J., Putnis, A., Geisler, T., Schmidt, B. C., & Golla-Schindler, U. (2010). The replacement of plagioclase feldspars by albite: observations from hydrothermal experiments. *Contributions to Mineralogy and Petrology*, 159(1), 43-59.
- Hyppolito, T., García-Casco, A., Juliani, C., Meira, V., & Hall, C. (2014). Late Paleozoic onset of subduction and exhumation at the western margin of Gondwana (Chilenia Terrane): Counterclockwise P–T paths and timing of metamorphism of deep-seated garnet–mica schist and amphibolite of Punta Sirena, Coastal Accretionary Complex, central Chile (34 S). *Lithos*, 206, 409-434.
- Imon, R., Okudaira, T., & Fujimoto, A. (2002). Dissolution and precipitation processes in deformed amphibolites: an example from the ductile shear zone of the Ryoke metamorphic belt, SW Japan. *Journal of Metamorphic Geology*, 20(3), 297-308.
- Imon, R., Okudaira, T., & Kanagawa, K. (2004). Development of shape-and lattice-preferred orientations of amphibole grains during initial cataclastic deformation and subsequent deformation by dissolution–precipitation creep in amphibolites from the Ryoke metamorphic belt, SW Japan. *Journal of Structural Geology*, 26(5), 793-805.
- +++AJackson, J., Austrheim, H., McKenzie, D., & Priestley, K. (2004). Metastability, mechanical strength, and the support of mountain belts. *Geology*, 32(7), 625-628.
- Janák, M., van Roermund, H., Majka, J., & Gee, D. (2013). UHP metamorphism recorded by kyanite-bearing eclogite in the Seve Nappe Complex of northern Jämtland, Swedish Caledonides. *Gondwana Research*, 23(3), 865-879.
- Jiang, Z., Prior, D. J., & Wheeler, J. (2000). Albite crystallographic preferred orientation and grain misorientation distribution in a low-grade mylonite: implications for granular flow. *Journal of Structural Geology*, 22(11), 1663-1674.
- Kanagawa, K., Shimano, H., & Hiroi, Y. (2008). Mylonitic deformation of gabbro in the lower crust: A case study from the Pankenushi gabbro in the Hidaka metamorphic belt of central Hokkaido, Japan. *Journal of Structural Geology*, 30(9), 1150-1166.

- Klonowska, I., Janák, M., Majka, J., Froitzheim, N., & Kościńska, K. (2016). Eclogite and garnet pyroxenite from Stor Jougdan, Seve Nappe Complex, Sweden: implications for UHP metamorphism of allochthons in the Scandinavian Caledonides. *Journal of Metamorphic Geology*, 34(2), 103-119.
- Klonowska, I., Janák, M., Majka, J., Petřík, I., Froitzheim, N., Gee, D., & Sasinková, V. (2017). Microdiamond on Åreskutan confirms regional UHP metamorphism in the Seve Nappe Complex of the Scandinavian Caledonides. *Journal of Metamorphic Geology*.
- Kruse, R., Stünitz, H., & Kunze, K. (2001). Dynamic recrystallization processes in plagioclase porphyroclasts. *Journal of Structural Geology*, 23(11), 1781-1802.
- Ladenberger, A., Be'eri-Shlevin, Y., Claesson, S., Gee, D. G., Majka, J., & Romanova, I. V. (2013). Tectonometamorphic evolution of the Åreskutan Nappe–Caledonian history revealed by SIMS U–Pb zircon geochronology. *Geological Society, London, Special Publications*, 390, SP390. 310.
- Lafrance, B., & Vernon, R. (1993). Mass transfer and microfracturing in gabbroic mylonites of the Guadalupe igneous complex, California. *Defects and processes in the solid state: geoscience applications: the McLaren volume (Developments in Petrology, Vol. 4)*. Amsterdam, Elsevier Science, 151-167.
- Lanari, P. (2012). *Micro-cartographie P-T-e dans les roches métamorphiques. Applications aux Alpes et à l'Himalaya*. (Doctorate PhD), Grenoble,
- Lanari, P., Guillot, S., Schwartz, S., Vidal, O., Tricart, P., Riel, N., & Beyssac, O. (2012). Diachronous evolution of the alpine continental subduction wedge: evidence from P-T estimates in the Briançonnais Zone houillère (France – Western Alps). *Journal of Geodynamics*, 56-57, 39-54.
- Lanari, P., Riel, N., Guillot, S., Vidal, O., Schwartz, S., Pêcher, A., & Hattori, K. H. (2013). Deciphering high-pressure metamorphism in collisional context using microprobe mapping methods: Application to the Stak eclogitic massif (northwest Himalaya). *Geology*, 41(2), 111-114.
- Lanari, P., Vidal, O., Lewin, E., Dubacq, B., De Andrade, V., & Schwartz, S. (2014). XMapTools a Matlab®-based graphic user interface for microprobe quantified image processing. *Computers and Geosciences*, 62, 227-240. doi:10.1016/j.cageo.2013.08.010
- Leake, B. E., Woolley, A. R., Arps, C. E., Birch, W. D., Gilbert, M. C., Grice, J. D., . . . Krivovichev, V. G. (1997). Report. Nomenclature of Amphiboles: Report of the Subcommittee on Amphiboles of the International Mineralogical Association Commission on New Minerals and Mineral Names. *Mineralogical Magazine*, 61(2), 295-321.
- Lee, M. R., Parsons, I., Edwards, P. R., & Martin, R. W. (2007). Identification of cathodoluminescence activators in zoned alkali feldspars by hyperspectral imaging and electron-probe microanalysis. *American Mineralogist*, 92(2-3), 243-253.
- Liou, J., Kuniyoshi, S., & Ito, K. (1974). Experimental studies of the phase relations between greenschist and amphibolite in a basaltic system. *American Journal of Science*, 274(6), 613-632.
- Lloyd, G. E., Farmer, A. B., & Mainprice, D. (1997). Misorientation analysis and the formation and orientation of subgrain and grain boundaries. *Tectonophysics*, 279(1-4), 55-78.
- Lorenz, H., Rosberg, J.-E., Juhlin, C., Bjelm, L., Almqvist, B. S. G., Berthet, T., . . . Pascal, C. (2015). COSC-1-drilling of a subduction-related allochthon in the Palaeozoic Caledonide orogen of Scandinavia. *Scientific Drilling*, 19, 1.
- Majka, J., Rosén, Å., Janák, M., Froitzheim, N., Klonowska, I., Manecki, M., . . . Yoshida, K. (2014). Microdiamond discovered in the Seve Nappe (Scandinavian Caledonides) and its exhumation by the “vacuum-cleaner” mechanism. *Geology*, 42(12), 1107-1110.
- Mariano, A., & King, P. (1975). Europium-activated cathodoluminescence in minerals. *Geochimica et Cosmochimica Acta*, 39(5), 649-660.
- Marti, S., Stünitz, H., Heilbronner, R., Plümper, O., & Drury, M. (2017). Experimental investigation of the brittle-viscous transition in mafic rocks—Interplay between fracturing, reaction, and viscous deformation. *Journal of Structural Geology*, 105, 62-79.

- McAleer, R., Bish, D., Kunk, M., Sicard, K., Valley, P., Walsh, G., . . . Wintsch, R. (2017). Reaction softening by dissolution–precipitation creep in a retrograde greenschist facies ductile shear zone, New Hampshire, USA. *Journal of Metamorphic Geology*, 35(1), 95-119.
- McLaren, A., & Pryer, L. (2001). Microstructural investigation of the interaction and interdependence of cataclastic and plastic mechanisms in feldspar crystals deformed in the semi-brittle field. *Tectonophysics*, 335(1), 1-15.
- Menegon, L., Füsseis, F., Stünitz, H., & Xiao, X. (2015). Creep cavitation bands control porosity and fluid flow in lower crustal shear zones. *Geology*, 43(3), 227-230.
- Menegon, L., Pennacchioni, G., & Spiess, R. (2008). Dissolution-precipitation creep of K-feldspar in mid-crustal granite mylonites. *Journal of Structural Geology*, 30(5), 565-579.
- Miyashiro, A. (1968). Metamorphism of mafic rocks. *Basalts*, 2, 799-834.
- Mouthereau, F., Lacombe, O., & Vergés, J. (2012). Building the Zagros collisional orogen: timing, strain distribution and the dynamics of Arabia/Eurasia plate convergence. *Tectonophysics*, 532, 27-60.
- Mouthereau, F., Watts, A. B., & Burov, E. (2013). Structure of orogenic belts controlled by lithosphere age. *Nature Geosci*, 6(9), 785-789. doi:10.1038/ngeo1902
<http://www.nature.com/ngeo/journal/v6/n9/abs/ngeo1902.html#supplementary-information>
- Mukai, H., Austrheim, H., Putnis, C. V., & Putnis, A. (2014). Textural evolution of plagioclase feldspar across a shear zone: implications for deformation mechanism and rock strength. *Journal of Petrology*, 55(8), 1457-1477.
- Newton, R. C., & Smith, J. (1967). Investigations concerning the breakdown of albite at depth in the earth. *The Journal of Geology*, 75(3), 268-286.
- Northrup, C. (1996). Structural expressions and tectonic implications of general noncoaxial flow in the midcrust of a collisional orogen: The northern Scandinavian Caledonides. *Tectonics*, 15(2), 490-505.
- Nyman, M. W., Law, R. D., & Smelik, E. A. (1992). Cataclastic deformation mechanism for the development of core-mantle structures in amphibole. *Geology*, 20(5), 455-458.
- Okudaira, T., Shigematsu, N., Harigane, Y., & Yoshida, K. (2017). Grain size reduction due to fracturing and subsequent grain-size-sensitive creep in a lower crustal shear zone in the presence of a CO₂-bearing fluid. *Journal of Structural Geology*, 95, 171-187. doi:<https://doi.org/10.1016/j.jsg.2016.11.001>
- Parsons, I., & Lee, M. R. (2009). Mutual replacement reactions in alkali feldspars I: microtextures and mechanisms. *Contributions to Mineralogy and Petrology*, 157(5), 641.
- Parsons, I., Steele, D. A., Lee, M. R., & Magee, C. W. (2008). Titanium as a cathodoluminescence activator in alkali feldspars. *American Mineralogist*, 93(5-6), 875-879.
- Passchier, C., & Trouw, R. (1996). Microtectonics: Springer Verlag. *Berlin, Germany*, 289.
- Pearce, M. A., Wheeler, J., & Prior, D. J. (2011). Relative strength of mafic and felsic rocks during amphibolite facies metamorphism and deformation. *Journal of Structural Geology*, 33(4), 662-675.
- Plümper, O., Botan, A., Los, C., Liu, Y., Malthe-Sørenssen, A., & Jamtveit, B. (2017). Fluid-driven metamorphism of the continental crust governed by nanoscale fluid flow. *Nature Geoscience*, 10, 685. doi:10.1038/ngeo3009
<https://www.nature.com/articles/ngeo3009#supplementary-information>
- Plümper, O., John, T., Podladchikov, Y. Y., Vrijmoed, J. C., & Scambelluri, M. (2017). Fluid escape from subduction zones controlled by channel-forming reactive porosity. *Nature Geosci*, 10(2), 150-156. doi:10.1038/ngeo2865
<http://www.nature.com/ngeo/journal/v10/n2/abs/ngeo2865.html#supplementary-information>
- Plümper, O., & Putnis, A. (2009). The complex hydrothermal history of granitic rocks: multiple feldspar replacement reactions under subsolidus conditions. *Journal of Petrology*, 50(5), 967-987.

- Prior, D. J., Wheeler, J., Peruzzo, L., Spiess, R., & Storey, C. (2002). Some garnet microstructures: an illustration of the potential of orientation maps and misorientation analysis in microstructural studies. *Journal of Structural Geology*, 24(6), 999-1011.
- Putnis, A. (2002). Mineral replacement reactions: from macroscopic observations to microscopic mechanisms. *Mineralogical Magazine*, 66(5), 689-708.
- Putnis, A. (2009). Mineral replacement reactions. *Reviews in Mineralogy and Geochemistry*, 70(1), 87-124.
- Putnis, A. (2015). Transient porosity resulting from fluid–mineral interaction and its consequences. *Reviews in Mineralogy and Geochemistry*, 80, 1-23.
- Putnis, A., & Putnis, C. V. (2007). The mechanism of reequilibration of solids in the presence of a fluid phase. *Journal of Solid State Chemistry*, 180(5), 1783-1786.
- Rice, A. H. N., & Anderson, M. W. (2016). Restoration of the external Scandinavian Caledonides. *Geological Magazine*, 1-30.
- Roberts, D. (2003). The Scandinavian Caledonides: event chronology, palaeogeographic settings and likely modern analogues. *Tectonophysics*, 365(1), 283-299.
- Roberts, D., & Gee, D. (1985). An introduction to the structure of the Scandinavian Caledonides. *The Caledonide orogen—Scandinavia and related areas*, 1, 55-68.
- Root, D., & Corfu, F. (2012). U–Pb geochronology of two discrete Ordovician high-pressure metamorphic events in the Seve Nappe Complex, Scandinavian Caledonides. *Contributions to Mineralogy and Petrology*, 163(5), 769-788.
- Royden, L. (1996). Coupling and decoupling of crust and mantle in convergent orogens: Implications for strain partitioning in the crust. *Journal of Geophysical Research: Solid Earth*, 101(B8), 17679-17705.
- Ruiz-Agudo, E., Putnis, C., & Putnis, A. (2014). Coupled dissolution and precipitation at mineral–fluid interfaces. *Chemical Geology*, 383, 132-146.
- Rutter, E. (1983). Pressure solution in nature, theory and experiment. *Journal of the Geological Society*, 140(5), 725-740.
- Rutter, E., & Brodie, K. (1992). Rheology of the lower crust. *Continental lower crust*, 201-267.
- Sjöström, H. (1983). The Seve—Köli Nappe Complex of the Handöl—Storlien—Essandsjøen area, Scandinavian Caledonides. *Geologiska Föreningen i Stockholm Förhandlingar*, 105(2), 93-117.
- Skrotzki, W. (1992). Defect structure and deformation mechanisms in naturally deformed hornblende. *physica status solidi (a)*, 131(2), 605-624.
- Smith, J., & Stenstrom, R. (1965). Electron-excited luminescence as a petrologic tool. *The Journal of Geology*, 73(4), 627-635.
- Spruzeniece, L., Piazzolo, S., & Maynard-Casely, H. E. (2017). Deformation-resembling microstructure created by fluid-mediated dissolution–precipitation reactions. *Nature Communications*, 8, 14032.
- Stephens, M. B. (1988). The Scandinavian Caledonides: a complexity of collisions. *Geology Today*, 4(1), 20-26.
- Stokes, M., Wintsch, R., & Southworth, C. (2012). Deformation of amphibolites via dissolution–precipitation creep in the middle and lower crust. *Journal of Metamorphic Geology*, 30(7), 723-737.
- Strand, T., & Kulling, O. (1972). *Scandinavian Caledonides*: John Wiley & Sons.
- Strömberg, A., Karis, L., Zachrisson, E., Sjöstrand, T., Skoglund, R., Lundegårdh, P., . . . Kornfält, K. (1984). Berggrundskarta över Jämtlands län utom förutvarande Fjällsjö kommun, scale 1: 200 000. *Geological Survey of Sweden, Ca*, 53.
- Tullis, J., Yund, R., & Farver, J. (1996). Deformation-enhanced fluid distribution in feldspar aggregates and implications for ductile shear zones. *Geology*, 24(1), 63-66.
- Van Roermund, H. (1985). Eclogites of the Seve nappe, central Scandinavian Caledonides. *The Caledonide Orogen—Scandinavia and Related Areas*, 873-886.

- Van Roermund, H. (1989). High-pressure ultramafic rocks from the allochthonous nappes of the Swedish Caledonides. *The Caledonide Geology of Scandinavia*, 205-219.
- Vidal, O., De Andrade, V., Lewin, E., Munoz, M., Parra, T., & Pascarelli, S. (2006). P–T-deformation-Fe³⁺/Fe²⁺ mapping at the thin section scale and comparison with XANES mapping: application to a garnet-bearing metapelite from the Sambagawa metamorphic belt (Japan). *Journal of Metamorphic Geology*, 24(7), 669-683.
- Vidal, O., Lanari, P., Munoz, M., Bourdelle, F., & De Andrade, V. (2016). Deciphering temperature, pressure and oxygen-activity conditions of chlorite formation. *Clay Minerals*, 51(4), 615-633.
- Vidal, O., Parra, T., & Vieillard, P. (2005). Thermodynamic properties of the Tschermak solid solution in Fe-chlorite: Application to natural examples and possible role of oxidation. *American Mineralogist*, 90(2-3), 347-358.
- Walker, F. D. L., Lee, M. R., & Parsons, I. (1995). Micropores and micropermeable texture in alkali feldspars: geochemical and geophysical implications. *Mineralogical Magazine*, 59(3), 505-534.
- Wallis, D., Phillips, R., & Lloyd, G. (2014). Evolution of the Eastern Karakoram Metamorphic Complex, Ladakh, NW India, and its relationship to magmatism and regional tectonics. *Tectonophysics*, 626, 41-52.
- Wassmann, S., & Stöckhert, B. (2012). Matrix deformation mechanisms in HP-LT tectonic mélanges—microstructural record of jadeite blueschist from the Franciscan Complex, California. *Tectonophysics*, 568, 135-153.
- Wassmann, S., & Stöckhert, B. (2013). Rheology of the plate interface—dissolution precipitation creep in high pressure metamorphic rocks. *Tectonophysics*, 608, 1-29.
- Wassmann, S., Stöckhert, B., & Trepmann, C. A. (2011). Dissolution precipitation creep versus crystalline plasticity in high-pressure metamorphic serpentinites. *Geological Society, London, Special Publications*, 360(1), 129-149.
- Wenning, Q. C., Berthet, T., Ask, M., Zappone, A., Rosberg, J. E., & Almqvist, B. S. (2017). Image log analysis of in situ stress orientation, breakout growth, and natural geologic structures to 2.5 km depth in central Scandinavian Caledonides: Results from the COSC-1 borehole. *Journal of Geophysical Research: Solid Earth*.
- Whitney, D. L., & Evans, B. W. (2010). Abbreviations for names of rock-forming minerals. *American Mineralogist*, 95(1), 185-187.
- Winkler, W. (1980). Petrogenesis of metamorphic rocks, 5th ed. *Springer-Verlag, New York*(1), 348 p.
- Wintsch, R., & Yi, K. (2002). Dissolution and replacement creep: a significant deformation mechanism in mid-crustal rocks. *Journal of Structural Geology*, 24(6), 1179-1193.
- Zachrisson, E., & Sjöstrand, T. (1990). Bedrock Map 22E Frostviken. *Sveriges Geologiska Undersökning (SGU) Ai 44*, scale 1: 50,000.

FIGURE 1 Geological setting of the Scandinavian Caledonides. (a) Tectonic map with inferred paleogeography of the nappes (modified after Gee, Juhlin, Pascal, & Robinson, 2010). (b) Cross section marked in (a) with vertical exaggeration of 5 x and approximate location of the COSC-1 borehole (modified after Gee et al., 2010). (c) Detail of the study area with location of the COSC-1 drilling site (modified after Strömberg et al., 1984).

FIGURE 2 Amphibolite with Pl porphyroclast displaying a mylonitic foliation defined by Amp, Pl, Chl, Qz, Ep and Ilm. Cal and Qz ribbons, presumably representing transposed veins, are parallel to the foliation. Both dextral- (clasts close to Figure 3 rectangle, marked by the white arrow) and sinistral sense of shear (C' planes, red dashed line) are visible. (a): plane-polarized light; (b): crossed-polarized light. Mineral abbreviation from Whitney and Evans (2010).

FIGURE 3 More detailed areas of sections shown in Figure 2. (a) Ab porphyroclasts with dark trails of inclusions of Ep and Cal few μm in size. The Ab porphyroclasts are wrapped by the mylonitic foliation defined by Amp, Olig and Chl. The white rectangle indicates the site of the EBSD map shown in Figure 7 (plane polarized light). (b) X-ray map showing Pl, Amp, Chl and Ep that crystallize in the pressure shadows of Ab porphyroclasts. (c) BSE image showing zoned Pl with dark cores (Pl1) and brighter rims (Pl2 and Pl3). Bright inclusions inside Pl are Ilm crystals. (d) CL image highlighting the difference between Ab cores (dark, Pl1) rimmed by Pl with higher An content (bright, Pl2 and Pl3). This bright Pl crystallizes also in the pressure shadows and in the fractures that dissect the Ab cores. (e) Standardized X-Ray map of the X Anorthite (XAn) in the Pl. Note the fractures in Pl1 sealed by Pl3 and sheared-off fragments of Pl1 rimmed by Pl2 and 3 (see text and Figure 5 for distinction). (f) Standardized X-Ray map of Amp crystals displaying relic cores higher in Mg# (Amp1) and rims lower in Mg# lengthened as the main foliation (Amp2). A minor but consistent shift toward higher Mg# is visible from the top to the bottom of the picture, probably related to an analytical artefact.

FIGURE 4 Details of the microstructures shown in Figure 3c. BSE images. (a) Dark Pl1, highlighted by the dashed yellow line, with lobate edges and peninsular features rimmed by Pl2 and Pl3. (b) Iso-oriented Ilm and Rt inclusions in Pl1. Note the two perpendicular trails of pores in Pl2 and Pl3. (c) Detail of the pore trails and associated Ms and Cal inclusions. (d) Close-up of (c) highlighting pores, abundant Ms inclusions and rare Ba-rich Ms.

FIGURE 5 Mineral chemistry of Pl, Amp and Chl. The subdivision in generations was made based on microtextures. (a) Pl groups based on the XAb and XAn content: Pl1 XAn 0-0.05; Pl2 XAn 0.05-0.13; Pl3 XAn 0.13-0.25. Compare with Figure 3e. (b) Amp groups based on the Mg# and Si apfu content: Amp1 Mg# 0.5-0.44, Si apfu 7-6.5; Amp2 Mg# 0.44-0.36, Si apfu 6.5-6.1. Compare with Figure 3f. (c) Compositional map of Chl Mg# for 0% Fe^{3+} . The crystals display homogeneous compositions (Chl1 Mg# 0.59-0.56), except at grain boundaries and along C' band where lower values are present (Chl2 Mg# 0.55-0.52) (d) Diagram of classification of calcic amphiboles with plotted the average chemical compositions of Amp1 and Amp2 (from Leake et al., 1997).

FIGURE 6 Chlorite+Quartz+H₂O thermometry results calculated at a pressure of 0.7 GPa and a range between 0-50 % of Fe^{3+} .

FIGURE 7 Details of the microstructure shown in Figure 3 (referred to as domain 1 in the text). (a) CL image of a dark Pl1 porphyroclast with fractures and rims containing the bright Pl2-3. (b) Standardized X-Ray map of the XAn content showing the overlap between the bright CL areas and the Pl2-Pl3 compositions. (c) EBSD GOS map superposed to the band contrast (BC) map of the same area shown in (a). White lines: low angle boundaries 2-10°. Black lines: high angle boundaries > 10°. Light blue lines: Twin boundaries in Pl. (d) EBSD texture component map (TCM) of the Pl1 porphyroclast, showing the misorientation from the reference point marked by the red cross. White lines: low angle boundaries 2-10°. Black lines: high angle boundaries > 10°. Light blue lines: Twin boundaries in Pl. (e) EBSD GOS of Amp from the area shown in (a). White lines: low angle boundaries 2-10°. Black lines: high angle boundaries > 10°. (f) EBSD TCM of Amp, showing the misorientation from the reference point marked by the red cross. White lines: low angle boundaries 2-10°. Black lines: high angle boundaries > 10°.

FIGURE 8 Details of Figure 2 (referred to as domain 2 in the text). (a) Light microscopy microstructure of the site analysed with EBSD. (b) CL image of the site shown in (a). Dark Pl1 porphyroclasts are overgrown by bright Pl2 and Pl3. (c) EBSD phases map of the site shown in (a). Note the epitaxial growth of Pl2 and Pl3 on Pl1, as indicated by the lack of high angle boundaries separating Pl1 from Pl2 and Pl3, and the very few low angle boundaries in the Pl1 porphyroclast. (d) EBSD TCM showing the misorientation from reference point (red cross) in Pl1 porphyroclasts. Note

the correlation between higher misorientation and PI2-PI3 overgrowth on the right-hand side of the reference point. (e) EBSD GOS map suggesting that the PI crystals are very low internal strain. (f) EBSD TCM showing the misorientation from reference point of another PI1 porphyroclast. (g) EBSD GOS map of Amp. (h) EBSD TCM showing the misorientation from reference point in an Amp crystal elongate parallel to the foliation.

FIGURE 9 Details of Figure 2. (a) Sigmoidal grain of Amp surrounded by Chl along the foliation wrapping around PI porphyroclasts. Several brittle fractures perpendicular to the Amp elongation are visible (plane-polarized light). The white rectangle encompasses the site of the EBSD maps shown in (d) and (f). (b) X-ray map of the mineral phases in (a). (c) Standardized X-Ray map showing the variation in Mg# of Amp grains (scale bar on the right-hand side). Amp displays cores higher in Mg# (Amp1) and rims lower in Mg# (Amp2) elongate parallel to the foliation (compare with Figure 3f). (d) EBSD GOS map of Amp. The black line is the trace of the misorientation profile a-b shown in (e). See (a) for the location of the map. (e) Misorientation profile a-b drawn across a low-angle boundary. (f) EBSD TCM showing the misorientation from the reference point marked by a red cross.

FIGURE 10 Pole figures of the crystallographic orientation data of PI (colour-coding as in the grain size maps) and Amp; same site as maps shown in Figure 8. X is the extensional instantaneous stretching axis, Z is the pole of foliation, stereographic projections, lower hemisphere if not specified; U: upper hemisphere, L: lower hemisphere. (a) Subset of the PI porphyroclast and adjacent grains sharing the same crystallographic orientation, with the exception of a few data points. The PI displays a CPO with the (100) and (001) maxima approximately at 45° from X. The (010) maximum is perpendicular to X. a: 189029 PI data points. (b) Subset of the PI crystals of the matrix (PI2 and 3) not adjacent to the porphyroclast. A weak CPO similar to Figure 11a is visible. 34676 PI data points. (c) Amp displaying a CPO with the (100) and [001] perpendicular and parallel to X, respectively. 671 Amp data points (one-point-per-grain). n=number of grains. Half width 10° and cluster size 5°, maximum value is given. Contouring is 1.

FIGURE 11 Pole figures of the crystallographic orientation data of PI (colour-coding as in the grain size maps) and Amp; same site as maps shown in Figure 7. (a) The PI displays a CPO with the (100) and (001) at low to medium angles to X. Note how the maximum of the values coincides with the porphyroclast values, in red. 357353 PI data points. (b) Subset of the PI porphyroclast and adjacent grains; some of the latter display a similar crystallographic orientation as the porphyroclast. 238333 PI data points (c) Pole figures of Amp displaying a strong CPO with the (100) and [001] perpendicular and parallel to X, respectively. 140 Amp data points (one-point-per-grain). n=number of grains. Half width 10° and cluster size 5°, maximum value is given. Contouring is 2. (d) Histogram of distribution of misorientation angles and misorientation axes of amphibole plotted in crystal coordinates. 3295 Amp data points. Dashed line: forbidden zone limit.

FIGURE 12 Idealized sketch of the deformation history of PI and Amp, colour-coding as in the compositional maps. (a) 1: PI1 porphyrocrysts grew including a foliation marked by Ep, Qz and Ilm. 2: Fracturing of the PI1 porphyrocrysts, mostly imposed along the (001) plane. 3: Fluid infiltration triggered mineral replacement by coupled dissolution-precipitation with topotaxial and pseudomorphic growth of PI2 and, successively, PI3 on PI1. Replacement occurred mostly along and in proximity of the fractures as well as at the edges of the crystals. PI3 nucleated also as newly grown grains in the matrix. (b) 1: Amp1 grew with a CPO. 2: Replacement of Amp1 by Amp2 by coupled dissolution-precipitation; topotaxial growth is suggested by the same CPO shared by the two generations. 3: Development of misorientation due to displacement along the fractures and along the cleavage planes.

TABLE 1: Metamorphic and deformation evolution of sample ICDP5054EX8E601.

TABLE 2 Representative average composition analysis (wt%) of Pl and Amp.

TABLE 3 Representative average composition analysis (wt%) of Chl.

TABLE 4 Results of Amphibole-Plagioclase geothermobarometry computed from the values of Table 2. Thermometer abbreviation: HB: Holland and Blundy (1994). Barometer abbreviations: BB: Bhadra and Bhattacharya (2007); AS: Anderson and Smith (1995). The favoured results are highlighted in bold (see Section 5.1 for details).

TABLE 1 Metamorphic and deformation evolution of sample ICDP5054EX8E601.

Minerals	Pre-main foliation	Main foliation	C' Planes			
Amp	----	=====				
Pl	<u>Ab Core</u>	Ab/Olig Rims				
Chl		=====	----			
Qz	=====	=====	----			
Cal	----	=====	----			
Ep	=====	----				
Ilm	=====	=====				

TABLE 2 Representative average composition analysis (wt%) of Pl and Amp.

	Pl			Amp	
	Core (Pl1)	Rim1 (Pl2)	Rim2 (Pl3)	Core (Amp1)	Rim (Amp2)
SiO ₂	68.21	62.95	64.99	43.52	41.62
TiO ₂	0.01	0.01	0.01	0.22	0.35
Al ₂ O ₃	19.08	24.37	21.55	13.21	15.42
FeO	0.03	0.03	0.06	18.41	18.56
MnO	0.00	0.00	0.00	0.17	0.17
MgO	0.00	0.00	0.00	8.34	7.37
CaO	0.11	4.30	2.30	11.42	10.72
Na ₂ O	12.34	8.93	10.47	1.72	2.02
K ₂ O	0.04	0.05	0.05	0.21	0.35
Sum	99.83	100.64	99.43	97.22	96.57
	Formulae based on 8 O			Formulae based on 23 anhydrous O	
Si	2.99	2.76	2.88	6.49	6.26
Ti	-	-	-	0.02	0.04
Al	0.99	1.26	1.12	2.33	2.73
Fe ³⁺	-	-	-	0.41	0.49
Fe ²⁺	-	-	-	1.89	1.85
Mn	-	-	-	0.02	0.02
Mg	-	-	-	1.86	1.65
Ca	0.01	0.20	0.11	1.83	1.73
Na	1.05	0.76	0.90	0.50	0.59
K	0.00	0.00	0.00	0.04	0.07
Sum	5.04	4.99	5.01	15.38	15.42
Mg#	-	-	-	0.45	0.41
XAn	0.01	0.21	0.11	-	-
XAb	0.99	0.79	0.89	-	-

TABLE 3 Representative average composition analysis (wt%) of Chl.

Chl	Chl1-High Mg#		Chl2-Low Mg#	
	0% XFe ³⁺	30% XFe ³⁺	0% XFe ³⁺	30% XFe ³⁺
SiO ₂	25.70	25.70	26.52	26.69
Al ₂ O ₃	22.33	22.34	21.70	21.69
FeO	22.00	21.98	22.60	22.41
Fe ₂ O ₃	-	0.02	-	0.21
MnO	0.15	0.15	0.15	0.14
MgO	16.43	16.43	15.37	15.42
CaO	0.02	0.02	0.03	0.03
Na ₂ O	0.01	0.01	0.01	0.02
K ₂ O	0.00	0.00	0.01	0.01
Sum	86.63	86.65	86.38	86.62
Formulae based on 14 anhydrous O				
Si	2.69	2.63	2.78	2.74
Al	2.75	2.70	2.68	2.62
Mg	2.56	2.51	2.41	2.36
Fe ³⁺	0.00	0.57	0.00	0.58
Fe ²⁺	1.92	1.32	1.98	1.35
Sum	9.92	9.73	9.85	9.65
Mg#	0.57	0.66	0.55	0.64

TABLE 4 Results of Amphibole-Plagioclase geothermobarometry computed from the values of Table 2. Thermometer abbreviation: HB: Holland and Blundy (1994). Barometer abbreviations: BB: Bhadra and Bhattacharya (2007); AS: Anderson and Smith (1995). The favoured results are highlighted in bold (see Section 5.1 for details).

Amp-Pl couples	Thermometer	Barometer	
	HB	BB	AS
Amp1-Pl1	392 °C	-	-
Amp1-Pl2	615 °C	0.97 GPa	0.87 GPa
Amp2-Pl3	605 °C	0.74 GPa	1.09 GPa

